

The public reporting burden for this collection of information is estimated to average 1 hour per response, including the time for reviewing instructions, searching existing data sources, gathering and maintaining the data needed, and completing and reviewing the collection of information. Send comments regarding this burden estimate or any other aspect of this collection of information, including suggestions for reducing this burden, to Washington Headquarters Services, Directorate for Information Operations and Reports, 1215 Jefferson Davis Highway, Suite 1204, Arlington VA, 22202-4302. Respondents should be aware that notwithstanding any other provision of law, no person shall be subject to any penalty for failing to comply with a collection of information if it does not display a currently valid OMB control number.
PLEASE DO NOT RETURN YOUR FORM TO THE ABOVE ADDRESS.

1. REPORT DATE (DD-MM-YYYY) 11-03-2019	2. REPORT TYPE Final Report	3. DATES COVERED (From - To) 1-Sep-2017 - 31-Aug-2018
-------------------------------------------	--------------------------------	----------------------------------------------------------

4. TITLE AND SUBTITLE Final Report: Investigation of Room Temperature Electron-Hole Liquid in Atomically Thin Semiconductors	5a. CONTRACT NUMBER W911NF-17-1-0483
	5b. GRANT NUMBER
	5c. PROGRAM ELEMENT NUMBER 611102

6. AUTHORS	5d. PROJECT NUMBER
	5e. TASK NUMBER
	5f. WORK UNIT NUMBER

7. PERFORMING ORGANIZATION NAMES AND ADDRESSES North Carolina State University 2701 Sullivan Drive Admin Svcs III, Box 7514 Raleigh, NC 27695 -7514	8. PERFORMING ORGANIZATION REPORT NUMBER
-----------------------------------------------------------------------------------------------------------------------------------------------------------------	------------------------------------------

9. SPONSORING/MONITORING AGENCY NAME(S) AND ADDRESS (ES) U.S. Army Research Office P.O. Box 12211 Research Triangle Park, NC 27709-2211	10. SPONSOR/MONITOR'S ACRONYM(S) ARO
	11. SPONSOR/MONITOR'S REPORT NUMBER(S) 71878-PH.3

12. DISTRIBUTION AVAILABILITY STATEMENT Approved for public release; distribution is unlimited.

13. SUPPLEMENTARY NOTES The views, opinions and/or findings contained in this report are those of the author(s) and should not be construed as an official Department of the Army position, policy or decision, unless so designated by other documentation.

14. ABSTRACT

15. SUBJECT TERMS

16. SECURITY CLASSIFICATION OF:	17. LIMITATION OF ABSTRACT	15. NUMBER OF PAGES	19a. NAME OF RESPONSIBLE PERSON Kenan Gundogdu
a. REPORT UU	b. ABSTRACT UU	c. THIS PAGE UU	19b. TELEPHONE NUMBER 919-513-3409

RPPR Final Report

as of 14-Mar-2019

Agency Code:

Proposal Number: 71878PH

Agreement Number: W911NF-17-1-0483

INVESTIGATOR(S):

Name: Kenan Gundogdu
Email: kgundog@ncsu.edu
Phone Number: 9195133409
Principal: Y

Organization: **North Carolina State University**

Address: 2701 Sullivan Drive, Raleigh, NC 276957514

Country: USA

DUNS Number: 042092122

EIN: 566000756

Report Date: 30-Nov-2018

Date Received: 11-Mar-2019

Final Report for Period Beginning 01-Sep-2017 and Ending 31-Aug-2018

Title: Investigation of Room Temperature Electron-Hole Liquid in Atomically Thin Semiconductors

Begin Performance Period: 01-Sep-2017

End Performance Period: 31-Aug-2018

Report Term: 0-Other

Submitted By: Kenan Gundogdu

Email: kgundog@ncsu.edu

Phone: (919) 513-3409

Distribution Statement: 1-Approved for public release; distribution is unlimited.

STEM Degrees:

STEM Participants:

Major Goals: Objective: Our main objective in this research to investigate the room temperature electron hole liquid state in 2D TMDC materials.

Optical excitations in semiconductors result in electron-hole pairs. The Coulomb interaction among these pairs of charges leads to neutral bond states called excitons. While at low densities excitons behave like a non-interacting gas, at high densities they undergo a phase transition into a liquid state, i.e., electron-hole liquid (EHL). This phase transition of quasiparticles in semiconductors resembles the gas to liquid condensation, which occurs in real ambient matter. EHL is a condensed state and incompressible. As a result, in this state of matter the excited electrons and holes achieve the limit of the highest possible density in a material.

1- Cryogenic limitations: EHL is an exotic electronic phase that is unique to certain semiconductors at cryogenic conditions. It is generally observed in semiconductors with multivalley band structure. The critical temperature for liquid formation scales with one tenth of exciton binding energy.

2- Room Temperature EHL: Our group discovered EHL formation in atomically thin MoS₂ at room temperature. The formation of EHL is evident in the progression of the photoluminescence spectra (Figure 2). Mainly the excitation shifts to lower energies as a result of first heating then bandgap renormalization at high density. Eventually the PL intensity increased about 5 folds with only 10% increase in the excitation fluence. Further increase in excitation fluence only increased the PL spot to enlarge spatially but peak intensity and the spectral width did not change, suggesting formation of a constant density EHL phase observed from both in spectral and spatial profiles.

In this work, we will investigate certain properties of the 2D materials that enable creation of a long-lived EHL state. The results of these studies will be essential for developing new optoelectronic applications based on 2D semiconductors sustaining high excitation density at and beyond room temperature. The research objectives for the proposed nine-month study are:

- 1- Detailed characterization of EHL formation process
- 2- Heat management and thermal relaxation during EHL state

Accomplishments: A- Major Activities:

Experimental Achievements

- 1- Building an Raman microscopy setup for measurement of evolution of temperature and material changes lattice

RPPR Final Report

as of 14-Mar-2019

during the EHL phase transition.

2- Time resolved photon counting for measurement of evolution of the excited population

B- Specific Objectives and Major Findings:

1-One of our objective was to use these experiments to study evolution of the heat and understanding its role in the EHL formation process. We performed Raman experiments at different excitation fluences as the material is driven to EHL phase. We found that material reaches to a certain heat (~480K) due to laser exposure. As a result it expands. The Raman modes report the temperature and the strain build up very clearly.

2- Material band structure evolution: We collaborated with Lex Kemper in NC State Physics Department. Kemper group calculated the band energy levels at different strain magnitudes. It turns out that before the EHL process, the bands become indirect with K band in the valance band having a higher energy compared to G (γ) band.

3- Evolution of the excited state population and the measurement of the EHL lifetime: We further performed time resolved photoluminescence (PL) experiments. Our results showed that while the lifetime of the EHL phase is longer than 100s ns, the PL emission from EHL phase ceases in 2 ns after the excitation is stopped. These results confirm that most carriers leading to EHL state are in indirect gaps. Moreover these results also indicate that, the increased emission of PL while the pump laser is on the sample, is due to increased radiative recombination efficiency of the small density of carriers in the direct gap.

Both the increased PL efficiency and the lifetime of the EHL state are very interesting observations. It is clear that materials electronic and optical properties evolve significantly during the EHL phase. The lifetime increases more than 2 orders of magnitude, and the radiative recombination increases significantly for carriers in the direct gap.

4- Excitation density: We measured the excitation density using multiple experimental observables. Our results suggests the material reaches $4 \times 10^{13} \text{ cm}^{-2}$ carriers during EHL phase. This excitation density can sustained during under laser exposure.

5- Achievement of EHL phase excitation using below gap photons. We succeeded to excite EHL phase using below gap photons. Our understanding of the role of strain and heating in EHL formation helped us to use this in a new approach to create EHL phase in 2D MoS₂, which can't be used for other bulk materials. Since we can heat the material and shift the band gap by exciting the material at the band edge, we achieved first heating of the material then creating an EHL phase using photons that are below the gap. Under normal conditions below gap excitation does not create more than 10^{10} cm^{-2} carriers, but in this case it lead to excitation of dense EHL.

C- Key Outcomes:

We now know the critical conditions for forming and maintaining EHL phase in 2D MoS₂. Unlike bulk conventional semiconductors our results show that EHL phase requires strain related material changes. This finding is important for further study of EHL formation and dissipation kinetics in 2D materials and its utilization for Army needs.

Training Opportunities: The funding from ARO was extremely useful for building 2 advanced optical characterization setups.

One research scientist, three graduate students, and one undergrad student is involved in learning the experiments, the details of EHL phase transition in semiconductors.

Although the funding is ended, the setups are functional and playing a vital role in material characterization.

The skills that are acquired involve,

Experimental design, optics, computer programming, advanced knowledge in condensed matter physics.

RPPR Final Report

as of 14-Mar-2019

Results Dissemination: Manuscripts:

- 1- Dense Electron-Hole Plasma Formation and Ultra-Long Charge Lifetime in Monolayer MoS₂ via Material Tuning
AW Bataller, R Younts, A Rustagi, Y Yu, H Ardekani, A Kemper, L Cao, K. Gundogdu Nano letters 2019, 19 (2), pp 1104–1111
- 2- Below Bandgap Excitation Leads to Catastrophic Ionization and Electron-Hole Liquid in Room-Temperature Monolayer MoS₂ - under review

Conference presentations:

- 1- "Electron-Hole Liquid Formation in Monolayer Semiconductors at Room Temperature" A Bataller, R Younts, K Gundogdu, APS march meeting 2019
- 2- "Catastrophic Ionization in Monolayer Transition Metal Dichalcogenides"
R Younts, A Bataller, H Ardekani, K Gundogdu
- 3- "Carrier dynamics in optically excited Fermi degenerate states in atomically thin TMDC semiconductors" K Gundogdu
Physical Chemistry of Semiconductor Materials and Interfaces XVII 10724, 1072411
- 4- Optically Excited Fermi Degenerate States in 2D TMDCs K. Gundogdu, SEUF 2018

Honors and Awards: Nothing to Report

Protocol Activity Status:

Technology Transfer: Nothing to Report

PARTICIPANTS:

Participant Type: Postdoctoral (scholar, fellow or other postdoctoral position)

Participant: Alex Bataller

Person Months Worked: 2.00

Funding Support:

Project Contribution:

International Collaboration:

International Travel:

National Academy Member: N

Other Collaborators:

Participant Type: Graduate Student (research assistant)

Participant: Melike Biliroglu

Person Months Worked: 3.00

Funding Support:

Project Contribution:

International Collaboration:

International Travel:

National Academy Member: N

Other Collaborators:

Participant Type: Graduate Student (research assistant)

Participant: Gamze Findik

Person Months Worked: 3.00

Funding Support:

Project Contribution:

International Collaboration:

International Travel:

National Academy Member: N

Other Collaborators:

ARTICLES:

RPPR Final Report

as of 14-Mar-2019

Publication Type: Journal Article Peer Reviewed: Y **Publication Status:** 1-Published

Journal: Nano Letters

Publication Identifier Type: DOI

Publication Identifier: 10.1021/acs.nanolett.8b04408

Volume: 19

Issue: 2

First Page #: 1104

Date Submitted: 3/11/19 12:00AM

Date Published: 1/1/19 5:00AM

Publication Location:

Article Title: Dense Electron–Hole Plasma Formation and Ultralong Charge Lifetime in Monolayer MoS

Authors: Alexander W. Bataller, Robert A. Younts, Avinash Rustagi, Yiling Yu, Hossein Ardekani, Alexander Kem

Keywords: Two-dimensional materials, MoS₂, transition metal dichalcogenides, dense electron?hole plasma, bandgap renormalization, direct to indirect bandgap transition

Abstract: Many-body interactions in photoexcited semiconductors can bring about strongly interacting electronic states, culminating in the fully ionized matter of electron?hole plasma (EHP) and electron?hole liquid (EHL). These exotic phases exhibit unique electronic properties, such as metallic conductivity and metastable high photoexcitation density, which can be the basis for future transformative applications. However, the cryogenic condition required for its formation has limited the study of dense plasma phases to a purely academic pursuit in a restricted parameter space. This paradigm can potentially change with the recent experimental observation of these phases in atomically thin MoS₂ and MoTe₂ at room temperature. A fundamental understanding of EHP and EHL dynamics is critical for developing novel applications on this versatile layered platform. In this work, we studied the formation and dissipation of EHP in monolayer MoS₂.

Distribution Statement: 1-Approved for public release; distribution is unlimited.

Acknowledged Federal Support: Y

Publication Type: Journal Article Peer Reviewed: Y **Publication Status:** 4-Under Review

Journal: Advanced Materials

Publication Identifier Type:

Publication Identifier:

Volume:

Issue:

First Page #:

Date Submitted: 3/11/19 12:00AM

Date Published:

Publication Location:

Article Title: Below Bandgap Excitation Leads to Catastrophic Ionization and Electron-Hole Liquid in Room-Temperature Monolayer MoS₂

Authors: Robert Younts, Alexander Bataller, Hossein Ardekani, Yiling Yu, Linyou Cao, Kenan Gundogdu

Keywords: Electron Hole Liquid, 2D TMDC, MoS₂

Abstract: Atomically thin materials exhibit exotic electronic and optical properties. Strong many-body interactions from the reduced dielectric environment lead to electronic phases that drastically change conductivity and optical response. These many-body interactions can give rise to the formation of collective states such as Mott metal insulator transitions, electron-hole liquids and plasmas, and excitonic condensates, which typically occur at cryogenic temperatures and high excitation densities. Here we demonstrate in monolayer MoS₂ at room temperature, a low-density (10¹⁰ cm⁻²) excitonic gas is formed with continuous wave (CW) below-gap optical excitation. A slight increase in the excitation fluence triggers a nanosecond phase transition into a dense electron-hole plasma state with three orders of magnitude higher carrier density. We show that while the material is in equilibrium with the CW excitation slight excitation increase leads to sudden formation of a dense EHL phase.

Distribution Statement: 1-Approved for public release; distribution is unlimited.

Acknowledged Federal Support: Y

RPPR Final Report
as of 14-Mar-2019

Dense Electron–Hole Plasma Formation and Ultralong Charge Lifetime in Monolayer MoS₂ via Material Tuning

Alexander W. Bataller,[†] Robert A. Younts,[†] Avinash Rustagi,[†] Yiling Yu,[‡] Hossein Ardekani,[†] Alexander Kemper,[†] Linyou Cao,[‡] and Kenan Gundogdu^{*,†}

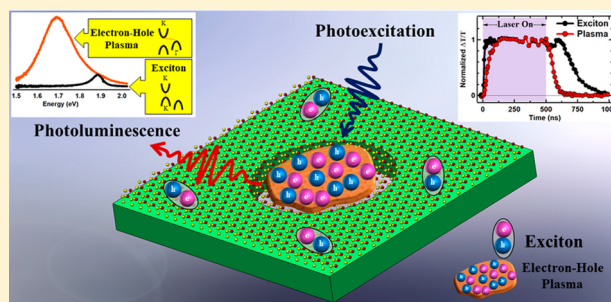
[†]Department of Physics, North Carolina State University, Raleigh, North Carolina 27695, United States

[‡]Department of Materials Science and Engineering, North Carolina State University, Raleigh, North Carolina 27695, United States

Supporting Information

ABSTRACT: Many-body interactions in photoexcited semiconductors can bring about strongly interacting electronic states, culminating in the fully ionized matter of electron–hole plasma (EHP) and electron–hole liquid (EHL). These exotic phases exhibit unique electronic properties, such as metallic conductivity and metastable high photoexcitation density, which can be the basis for future transformative applications. However, the cryogenic condition required for its formation has limited the study of dense plasma phases to a purely academic pursuit in a restricted parameter space. This paradigm can potentially change with the recent experimental observation of these phases in atomically thin MoS₂ and MoTe₂ at room temperature. A fundamental understanding of EHP and EHL dynamics is critical for developing novel applications on this versatile layered platform. In this work, we studied the formation and dissipation of EHP in monolayer MoS₂. Unlike previous results in bulk semiconductors, our results reveal that electromechanical material changes in monolayer MoS₂ during photoexcitation play a significant role in dense EHP formation. Within the free-standing geometry, photoexcitation is accompanied by an unconstrained thermal expansion, resulting in a direct-to-indirect gap electronic transition at a critical lattice spacing and fluence. This dramatic altering of the material's energetic landscape extends carrier lifetimes by 2 orders of magnitude and allows the density required for EHP formation. The result is a stable dense plasma state that is sustained with modest optical photoexcitation. Our findings pave the way for novel applications based on dense plasma states in two-dimensional semiconductors.

KEYWORDS: Two-dimensional materials, MoS₂, transition metal dichalcogenides, dense electron–hole plasma, bandgap renormalization, direct to indirect bandgap transition



The reduced dimensionality and dielectric screening for monolayer and few-layer transition metal dichalcogenides (TMDs) results in strong charge coupling and bound electron–hole pairs (excitons). For example, the binding energy between charge pairs is so strong (~ 0.5 eV) that excitons can exist well above room temperature.^{1–3} As a result, these materials provide a new test bed for studying many-body Coulomb systems. An exciting manifestation of this is the recent discovery of Fermi liquid condensation at room temperature.^{4–6} Although its existence has been known for nearly 50 years, the practical utilization of electron–hole plasma (EHP) and electron–hole liquid (EHL) has been hindered, due primarily to the cryogenic requirements for bulk semiconductors.⁷ Freed from this restrictive condition, atomically thin TMDs offer the potential of EHP-based applications.

Here we report the electronic, optical, and mechanical changes during formation and dissipation of dense EHP in monolayer MoS₂. We utilized time-resolved photoluminescence and transmission to study the evolution of optical excitations between excitonic and dense plasma states and the photoexcited carrier lifetime. In addition, we used Raman

spectroscopy combined with electronic band structure theory to study changes in the electronic band structure during the phase transition. Our studies reveal that the plasma phase transition in monolayer MoS₂ is a very intriguing process that involves changes in electronic band structure, recombination kinetics, and carrier lifetime. As illustrated in panels a and b of Figure 1, laser heating leads to material expansion accompanied by a direct-to-indirect gap transition. Optically excited carriers survive in the indirect gap for hundreds of nanoseconds, which promotes a high charge density and subsequent EHP formation (Figure 1c). While it is expected that the indirect gap formation should reduce the photoluminescence (PL) efficiency, we found that a small fraction of carriers that exist in the direct gap valleys radiatively recombine with a very high efficiency leading to observation of an unusual increase in the PL intensity in the EHP phase.

Received: November 1, 2018

Revised: December 21, 2018

Published: January 4, 2019

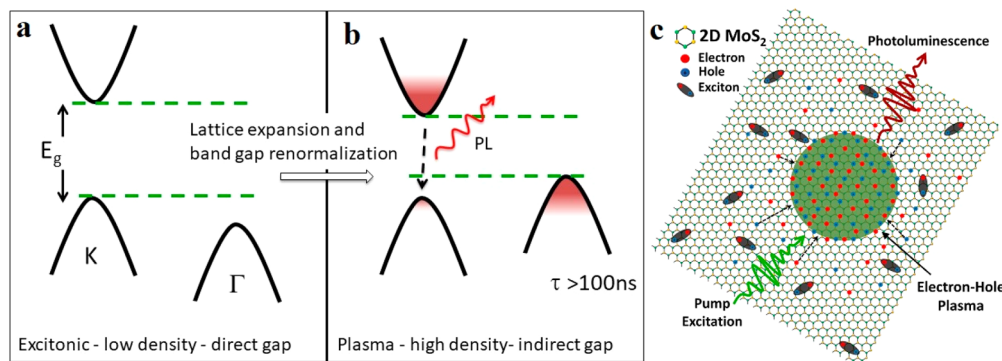


Figure 1. (a) Electronic band alignment for K and Γ valleys in MoS₂. (b) Under high photoexcitation, thermal expansion from material heating leads to an indirect bandgap formation with the conduction band minimum in the K valley and valence band maximum in the Γ valley. The long-lived (>100 ns) indirect charges allow the formation of (c) a highly ionized electron–hole plasma at room temperature.

Figure 2a shows PL spatial images under continuous-wave (CW) photoexcitation at various fluences. In this experiment, a

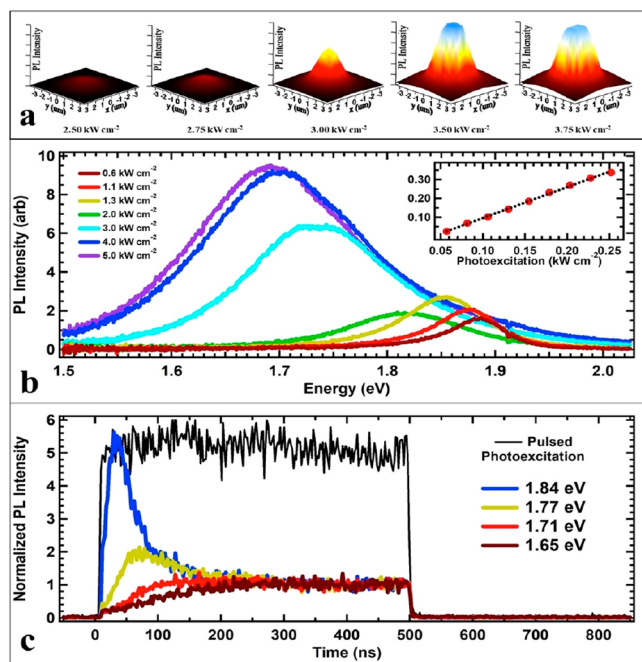


Figure 2. (a) Photoluminescence images of suspended monolayer MoS₂ under spatially uniform, steady-state photoexcitation at intensities below and above EHP formation. (b) Photoluminescence spectra measured from a 2 μm^2 area in the center of the suspended material with increasing photoexcitation. The inset shows the integrated PL vs photoexcitation at low fluence. (c) Time-resolved photoluminescence measured at different energy channels with 500 ns square-wave photoexcitation (637 nm). The photoexcitation intensity was 50% above the EHP threshold. All energy channels are normalized to the steady-state EHP intensity averaged between 300 and 500 ns. The instrument response function measured at 637 nm shows a 2 ns photoexcitation rise/fall (black curve).

CW laser is focused onto monolayer MoS₂ suspended over a 6 μm cavity (see Methods for sample preparation), and the resulting PL is collected using a microscope objective. As photoexcitation is increased, the PL intensity rapidly undergoes a transition from relatively weak excitonic emission to a bright, broadband, and dense EHP phase.^{4,8–10} When the photoexcitation density reaches a critical value, an 18%

increase in laser power results in a 540% stronger PL. Figure 2b shows the PL spectral evolution with increased photoexcitation as the phase transition takes place with high excitation fluence. At low fluence (inset of Figure 2b), the system is purely excitonic as evidenced by the linear relationship between the integrated PL and the photoexcitation (see Figure S1 for low-power spectra). As the carrier density increases, bandgap renormalization (BGR) induces a large spectral red-shift.¹¹ As detailed in earlier work,⁴ the transition occurring at ~ 3 kW cm⁻² is ascribed to the formation of a dense plasma state at 450 K with a carrier density of $\sim 4 \times 10^{13}$ cm⁻² (see the Supporting Information). All spectral features (width, location, and intensity) are unchanging beyond the critical intensity, indicating a constant carrier density, which could be evidence of dense plasma condensation, i.e., EHL.⁷

The dramatic increases in PL intensity and carrier density with only a slight (18%) increase in photoexcitation suggest a phase transition accompanied by a much longer carrier lifetime. First, the increase in PL indicates a reduction in nonradiative recombination. Second, carrier recombination and photogeneration rates are balanced under steady-state excitation, i.e., dynamic equilibrium. In the limit of slow carrier diffusion, as is the case for monolayer MoS₂,¹² the dynamic equilibrium condition can be written to first order as $\frac{aI}{E} = \frac{n}{\tau}$, where a is the absorption coefficient, I is the laser intensity, E is the photon energy, n is the carrier density, and τ is the carrier lifetime. To satisfy this equality under threshold conditions ($I = 3$ kW cm⁻², $a = 5\%$, $E = 2.33$ eV, and $n = 4 \times 10^{13}$ cm⁻²), the carrier lifetime must be around 100 ns. Given the reported exciton lifetime in MoS₂ (~ 1 ns),^{13,14} this remarkable finding suggests a massive change in carrier behavior exemplified by a lifetime that is 2 orders of magnitude longer.

To study EHP formation, we first characterized the carrier lifetime using time-resolved PL experiments (trPL) via time-correlated single-photon counting. Figure 2c shows PL evolution at four different photon energies when the material is excited using 500 ns square-wave laser pulses at 637 nm with an intensity 50% above the EHP threshold for CW conditions (3 mW). Upon photoexcitation, fast-rising emission associated with exciton recombination (1.84 eV in Figure 2c) dominates the spectrum. The excitonic emission then transfers spectral weight to the broadband EHP state (1.65 eV in Figure 2c) in ~ 100 ns. The PL reaches a steady-state condition at ~ 300 ns; i.e., the spectrum is unchanging. Surprisingly, once photoexcitation ceases at 500 ns, the PL is extinguished within the

experimental resolution (<2 ns) for all measured photon energies. The immediate disappearance of the PL appears to contradict the spectrally derived carrier density due to the apparent short PL lifetime. In other words, either the carrier density is grossly overestimated or long-lived carriers cease to radiatively recombine after photoexcitation steps.

To investigate the potential reasons behind the sudden disappearance of the emission during the trPL experiment, we studied changes in the material's electronic band structure using a combination of experimental Raman spectroscopy and theoretical electronic band structure calculations. Raman spectroscopy measures strain and temperature due to lattice expansion and laser heating, respectively. For monolayer MoS₂, the in-plane E' and out-of-plane A₁ Raman modes are sensitive to lattice spacing, where the former is primarily used to infer strain.^{15,16} These modes are shown in panels a and b of Figure 3 for both anti-Stokes and Stokes scattering as a function of photoexcitation. Two important trends are observed with increasing photoexcitation: (1) a spectral red-shifting and (2) a relative increase in the anti-Stokes intensity. A Lorentzian profile is fit to the E' mode whose peak position is plotted versus laser intensity in Figure 3c. Using the calibrated results of Lloyd et al.,¹⁷ the peak position is converted to a lattice

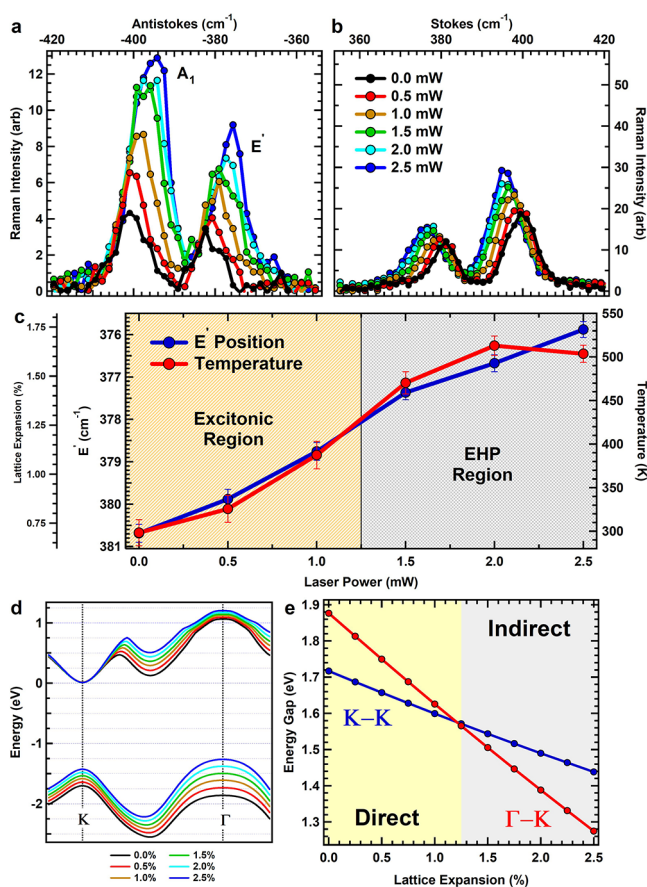


Figure 3. Raman spectrum for (a) anti-Stokes and (b) Stokes scattering as a function of 637 nm photoexcitation. (c) Power dependence of the lattice temperature (right axis) and expansion (left axis) determined by Raman anti-Stokes to Stokes ratio and E' peak position analysis, respectively. (d) Calculated electronic band structure from density functional theory calculations for different lattice expansion values. (e) Calculated bandgap energy for direct (K–K, blue curve) and indirect (Γ –K, red curve) valleys.

expansion. The material is found to have a positive prestrain with no photoexcitation, which is likely a result of the transfer process. The material temperature is obtained by comparing the Stokes and anti-Stokes intensity ratio through a Boltzmann factor (see the Supporting Information) and is plotted in Figure 3c. The shaded regions in Figure 3c represent the exciton and EHP phases as determined by the PL spectrum. Raman analysis at the EHP threshold indicates a material temperature of ~ 425 K accompanied by a lattice expansion of $\sim 1.25\%$ from photothermal expansion. We note that the measured lattice temperature using this Raman method matches our earlier result obtained using PL analysis.⁴

Experiments and density functional theory (DFT) calculations show strain, or in our case thermal expansion, has a significant impact on the material's electronic band structure, including a direct-to-indirect transition.^{18–20} Figure 3d shows the evolution of the calculated electronic band structure as a function of biaxial lattice expansion. As the lattice ions move farther apart, the energy of the indirect Γ valley increases relative to that of the direct K valley. Via comparison of the K–K and Γ –K energy gaps plotted in Figure 3e, a direct-to-indirect transition is expected for an expansion of 1.25%, thus showing a strong correlation with the onset of EHP formation (see Figure 3c). Fully formed EHP ($\sim 1.75\%$ expansion) shows a sizable indirectness as the Γ –K energy gap is ~ 70 meV lower than the K–K energy gap. Therefore, the EHP state in monolayer MoS₂ is found in a material with an indirect bandgap. Carrier recombination for an indirect gap semiconductor is mostly nonradiative and thus absent in the trPL for times after photoexcitation. The situation during continuous photoexcitation is similar, except carriers are created within the direct bandgap and can contribute to the PL prior to scattering into the lower-energy indirect valleys.

Because the material becomes an indirect gap semiconductor, the PL experiments are not effective in measuring the carrier population that is potentially surviving in the indirect bands. We measured the population of these “dark” carriers and their dynamics using differential transmission spectroscopy. This experiment measures the change in broadband optical transmission (“probe”) due to sample photoexcitation (“pump”). The pump pulse excites the sample and drives the system from excitonic to dense plasma states. The relative transmission of the probe pulse changes with respect to the unexcited sample. Because transmission depends on the availability of states, this experiment is sensitive to carrier populations regardless of whether they can radiatively recombine. Figure 4a shows the differential transmission's spectral evolution for MoS₂ driven to EHP. Spectral line-outs shown in panels b and c of Figure 4 reveal four distinct features and are attributed to bound and unbound (“free”) charge states. The two features at 1.90 and 2.04 eV are the A and B excitons, respectively.^{21–23} These excitonic transitions are situated entirely within the K valley and are energy-separated by spin–orbit coupling.²⁴ Because excitonic transitions are photobleached at a high carrier density, the intensity of the differential transmission signal increases at these spectral positions.²³ The negative transmission signal below 1.85 eV and above 2.15 eV arises from the conduction band red-shift due to the high density of free charges, i.e., bandgap renormalization.^{25–27} In other words, closing of the electronic bandgap due to BGR opens more absorption pathways at lower energies relative to the unexcited material, which results in a transmission decrease below 1.85 eV. The same effect

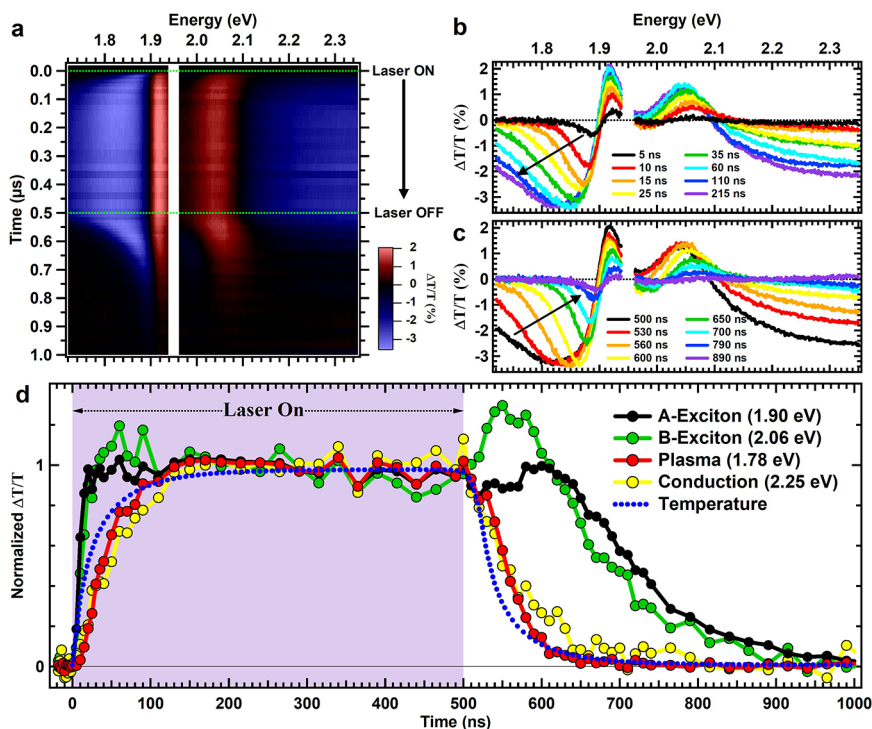


Figure 4. (a) Time-resolved differential transmission spectrum with 500 ns square-wave photoexcitation (green dashed lines). Spectral line-outs at various times during (b) EHP formation and (c) decay. (d) Temporal line-outs are shown at A (black) and B (green) exciton energies and at energies corresponding to dense plasma (red) and conduction band (yellow) states affected by bandgap renormalization. The temperature (blue dashed) dynamics for the material center is shown alongside the differential transmission. All energy channels are normalized to the steady-state EHP intensity averaged between 300 and 500 ns.

causes increased absorption above 2.15 eV due to the monotonically increasing absorption with respect to energy.

Figure 4d shows the temporal evolution corresponding to each of the excited species. To visualize the contrast between time evolutions of each species, we plot the absolute value of $\Delta T/T$. All spectral features grow with the onset of laser excitation until a saturation is reached at ~ 200 ns. Likewise, signal decay begins once photoexcitation ceases at 500 ns, after which all signals eventually relax back to zero. All curves are normalized to the average EHP-state value (300–500 ns). The temporal line-outs in Figure 4d show a significant difference in the growth and decay time scales between excitonic and free charge states, the former rising nearly as fast as the photoexcitation (< 10 ns) and the latter in > 100 ns. Because most exciton recombination and other microscopic processes in monolayer MoS_2 occur on subnanosecond time scales, we consider changes in lattice temperature as the primary cause for the slow rise and fall in the free charge states. This conclusion is further supported by comparing temperature dynamics calculated from a simplified heat diffusion model with the free charge dynamics in Figure 4d (see the Supporting Information). Therefore, the growth of dense plasma coincides with photothermal expansion and the transition to an indirect bandgap. More importantly, charge carriers remain in the material long after photoexcitation has ceased and much longer than the direct valley exciton lifetime (< 10 ns).¹³

Both the differential transmission and the Raman experiments indicate that electrons and holes mostly occupy an indirect gap when EHP is reached. Generally, radiative recombination is suppressed for an indirect gap semiconductor. Thus, our experiments should show a decrease in PL emission when the direct-to-indirect transition occurs.

However, the steady-state PL measurement in panels a and b of Figure 2 shows the PL emission intensity increasing > 5 -fold at the EHP threshold. It appears that while most of the carriers occupy an indirect valley, the carriers that radiatively recombine in the direct valley do so with a surprisingly high efficiency. In the CW PL measurements (Figure 2a,b), a fraction of the carriers will always occupy the direct gap because the (continuous) photoexcitation originates in the direct K–K band.

To further reveal the long-lived “dark” carriers, we performed an additional trPL experiment. We photoexcite the system to the EHP phase in the same manner described previously (cf. Figure 2c), but an additional CW “probe” laser at 532 nm is added to this experiment and focused to the same spatial location as the photoexcitation laser. The sole function of the probe laser is to add a continuous “trickle” of charges into the direct bandgap. Although many of these additional carriers will scatter into the indirect gap, some will radiatively recombine in the direct gap, thereby revealing the spectral evolution of the system’s energy levels. The probe power was 10-fold lower than the pulsed photoexcitation to prevent any significant perturbation to the EHP formation and decay process. Indeed, the PL dynamics with the added CW laser (Figure 5a) have very similar formation dynamics for the case of no CW excitation (Figure 2c). Unlike Figure 2c, there are significant deviations in the trPL signal after photoexcitation (> 500 ns), which supports the long-lived charge carrier observation in the transmission experiment.

Figure 5b reveals the PL time evolution at different spectral positions after the pump pulse has ceased. The low energy emission that we associate with EHP (1.65 eV) persists for > 150 ns after pump extinction without photoexcitation.

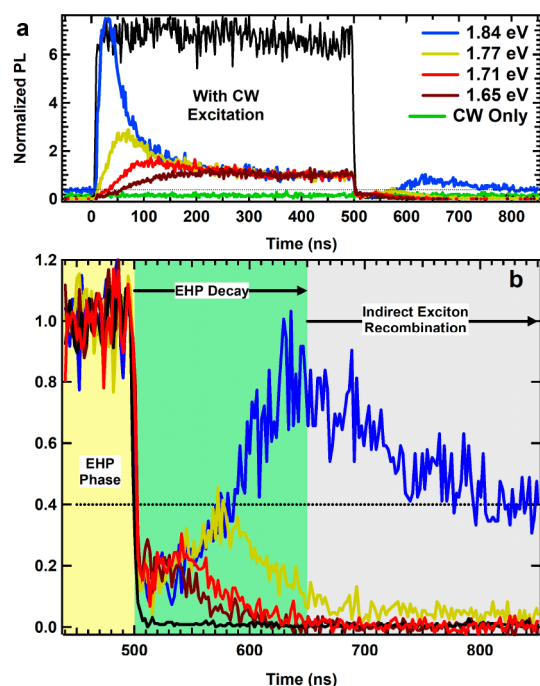


Figure 5. (a) Time-resolved photoluminescence measured at different energy channels with 500 ns square-wave photoexcitation (637 nm) and CW photoexcitation (532 nm). The 637 nm photoexcitation intensity was 50% above the EHP threshold (3 mW), and the 532 nm photoexcitation was 10 times weaker (0.3 mW). All energy channels are normalized to the steady-state EHP intensity averaged between 300 and 500 ns. Photoluminescence at the exciton energy channel (1.84 eV) with CW-only photoexcitation is shown as the green curve. The instrument response function measured at 637 nm shows a 2 ns photoexcitation rise/fall (black curve). Once excited to EHP, the overall exciton energy channel (blue) is offset by a factor of ~ 2 (black dashed). (b) Photoluminescence after pulsed photoexcitation showing EHP decay dynamics and long-lived charge lifetime.

Coinciding with the EHP decay, the excitonic emission (1.84 eV) increases for 150 ns, which is consistent with thermal

contraction and reduced BGR. At 650 ns, the spectral shift ends and the PL emission is dominated by exciton recombination, which eventually decays in >300 ns. Remarkably, the brightness of the exciton emission at 650 ns is double the long time, no photoexcitation value (black dashed vs blue curve in Figure 5b). If the only carriers in the material are created by the CW probe laser, then the PL emission should not rise above the equilibrium value and should decrease due to the elevated temperature and strain.^{28,29} Therefore, this observation must be linked to the presence of long-lived indirect carriers.

It should be noted that the excitonic PL is higher for $t < 0$ compared to CW-only (blue and green curves in Figure 5a) excitation. Therefore, driving the system to EHP has a long-term effect ($>200 \mu\text{s}$ given the 5 kHz repetition rate) on the material in the form of a higher PL efficiency. A possible mechanism is through the temporary p-doping of sulfur vacancies made available from the free charge states at high excitation. Although previous studies have shown similar photodoping effects,^{30,31} the question of whether it is present in this system remains open.

The optical diagnostics employed in this study not only paint a picture of the changing energetic landscape when monolayer MoS₂ is driven to EHP formation, they also indicate that the observed changes are unlikely due to defect states. First, the results are reproducible across numerous samples and with multiple power sweeps on the same material. If the PL transition was due to defect formation at high photoexcitation, we should not observe a threshold behavior in the second or later power sweeps. Instead, we observe a consistent threshold behavior for every power sweep across all measured suspended monolayers. Second, the Raman and low-power PL spectrum undergoes almost no change after photoexcitation.⁴ Furthermore, none of the reported defects in the scientific literature fully match the PL trends reported in this work in spectrum, temperature, and photoexcitation. Commonly reported defect states in MoS₂ originate from sulfur vacancies,^{32,33} oxygen treatment,³⁴ bright edge states,^{35,36} and laser cleaning.³⁷ However, we can generally exclude these defects as a cause

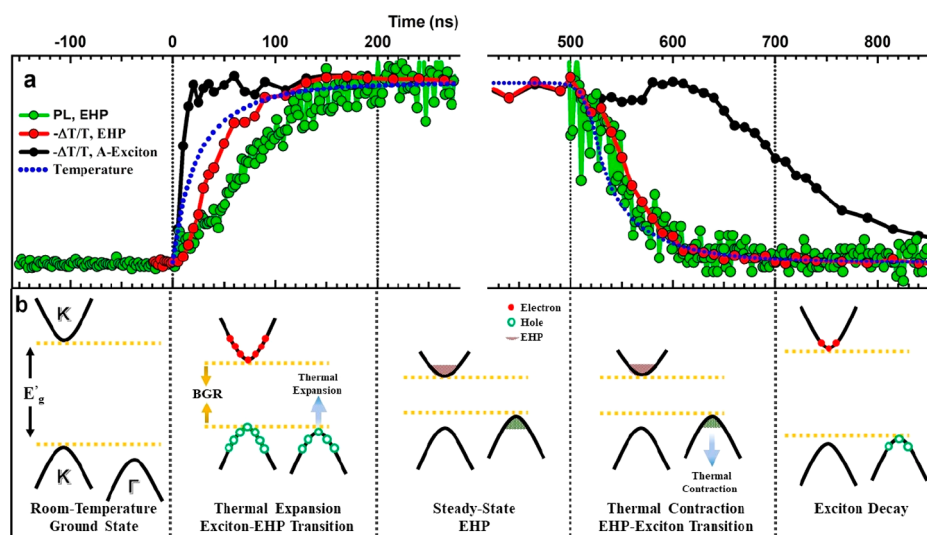


Figure 6. (a) Summary of optical dynamics. EHP response shown by time-resolved photoluminescence at 1.65 eV (green) and time-resolved differential transmission at 1.78 eV (red), excitonic response at 1.90 eV (black), and temperature dynamics from a heat diffusion model (blue dashed). All curves are normalized to the steady-state EHP condition averaged between 300 and 500 ns. (b) Electronic band diagram depicted at all phases of EHP formation and decay.

for the anomalous PL increase due to the phenomenon's reversibility and negligible material change. Specifically, sulfur vacancy emission is most prominent at low temperature, which is unlike the dramatic PL increase at elevated temperature in this system. Monolayer MoS₂ treated with oxygen plasma shows PL quenching with an increased level of exposure and little change in the spectral line shape.³⁴ Although bright edge states formed by oxygen annealing show a large PL enhancement, it is only observed at the exciton peak (1.85 eV) with no significant spectral broadening.^{35,36} Lastly, the process of laser cleaning at elevated photoexcitation requires treatment for minutes and produces a narrow excitonic PL,³⁷ rather than the broadband and near-instantaneous spectrum reported here.

The diagram presented in Figure 6b illustrates the changes in the material's band structure and charge population dynamics, separated into five distinct steps. The material begins its journey ($t < 0$) in the electronic ground state (no free charges), at room temperature (293 K), and has a direct bandgap (K–K). Laser excitation beginning at $t = 0$ provokes an immediate growth in exciton density (K–K), which is accompanied by BGR. The dynamic equilibrium of the excitons is soon established (10–20 ns), where charge creation and annihilation are in balance. The majority of absorbed light is converted into heat, as nonradiative recombination dominates monolayer MoS₂ under these conditions.¹³ The resulting temperature increase causes the material to undergo thermal expansion ($0 \text{ ns} < t < 200 \text{ ns}$) and lifts the valence Γ band above the K band. As the direct-to-indirect transition continues, charges are transferred into the Γ valley whose extended lifetime precipitates the high charge density and stability required for EHP formation. The system maintains EHP for as long as photoexcitation and laser heating are supplied (500 ns in our case). The cessation of photoexcitation at $t = 500 \text{ ns}$ begins the system's relaxation phase that is defined by material cooling, lattice contraction, and charge recombination. The fact that EHP persists for >50 ns without photoexcitation and shows no trace of radiative recombination suggests it resides entirely within the Γ valley. The excitation cycle ends with a slow decay phase ($\sim 1 \mu\text{s}$) defined by indirect exciton recombination occurring after EHP has died off and the material has cooled back to room temperature ($\sim 700 \text{ ns}$).

The surprising observation of enhanced photoluminescence accompanying a direct-to-indirect bandgap transition highlights a long-standing topic within the field of dense semiconductor plasma. Nonradiative pathways, i.e., Auger recombination, should be enhanced at a higher charge density and lead to shorter lifetimes; thus, contrary to our results, one would expect a reduced PL. However, earlier studies of carrier recombination dynamics show that in optically excited Fermi degenerate indirect bandgap semiconductors, normal Auger recombination is highly suppressed due to energy and momentum conservation.³⁸ As a result, a dense plasma state can exhibit both an increased lifetime and a high carrier density, both of which are observed in our experiments. The EHP in our study does indeed satisfy the Fermi degenerate condition, $T_F/T = n\pi\hbar^2/mkT \approx 6 > 1$, where a factor of 2 for spin has been included. We believe our results will help stimulate further theoretical and experimental efforts in the investigation of photoexcitation dynamics under degenerate conditions in two-dimensional materials.

The energetic roller coaster driving room-temperature EHP points toward a rich, dynamic system whose material

properties can be tuned and reset at MHz frequencies. It remains to be seen just how long EHP can persist in monolayer TMDs after photoexcitation has ended, using the appropriate lattice conditions, material combination, and photoexcitation scheme. The understanding of dynamic electronic structure and its effects on charge excitation will guide future efforts in generating and manipulating high-carrier density electronic states using ultrafast photoexcitation, and will help in engineering favorable geometries for high-power optoelectronic devices.

Methods. Sample Preparation. Complete details of the growth and transfer process can be found in ref 4. Briefly, CVD-grown monolayer MoS₂ was transferred onto a chemically etched quartz substrate. The quartz substrate was patterned with an array of 6 μm diameter cavities using photolithography and dry etching. The transfer process entailed dissolving polystyrene in toluene, followed by spin-coating on the as-grown monolayer, followed by baking for 1 h at 80–90 °C. A water droplet was placed on the polystyrene–monolayer assembly for substrate delamination, after which the monolayer was transferred to the quartz substrate. This was followed by another 1 h bake and removal of the polystyrene with a toluene rinse. All measurements were performed under vacuum conditions (30 mTorr).

CW Photoluminescence. CW photoluminescence was performed using a 532 nm TEM00 diode laser (Verdi, Coherent) focused 45° relative to the sample's surface. The measured spot size at the sample's surface was 35 μm [full width at half-maximum (fwhm)], thus providing a near-uniform intensity profile across the 6 μm suspension. Photoluminescence was collected by a 50 \times microscope objective and sent through a 570 nm long-pass filter. The photoluminescence was imaged onto the entrance slit of a spectrometer (Acton) using a 2 \times tube lens for a total of 100 \times magnification. Spatial–spatial (Figure 1a) and spatial–spectral images were recorded using a deep-cooled CCD instrument (PIXIS, Princeton Instruments). Spectra in Figure 1b were extracted from the spatial–spectral images in a 2 μm^2 area located at the center of the suspended region. See Figure S6 for the experimental diagram.

Time-Resolved Photoluminescence. Time-resolved photoluminescence (trPL) was photoexcited using a 637 nm TEM00 diode laser (OBIS, Coherent) focused through a 50 \times microscope objective to a 1.6 μm spot size (fwhm) in the center of the suspended region. The laser was triggered on and off using TTL pulses from a delay generator (DG535, Stanford Research Systems). The resulting laser pulse was a square wave with a 2 ns rise, a 500 ns on time, and a 2 ns fall and was repeated at 50 kHz (2.5% duty cycle). Photoluminescence was collected by the same 50 \times microscope objective and passed through a 638 nm notch filter. The photoluminescence wavelength was selected using a monochromator (5 nm bandwidth) and then detected using a PMT instrument (H10721-20, Hamamatsu). The temporal resolution was obtained by sending timing signals from the delay generator (“start”) and PMT instrument (“stop”) to a custom-built time-correlated single-photon counting (TCSPC) system. Although the TCSPC resolution was 200 ps, the experimental timing was ultimately limited to 2 ns determined by the laser rise/fall time. See Figure S7 for the experimental diagram.

Raman Spectroscopy. Raman spectroscopy was performed using the same photoexcitation laser (637 nm) as the trPL, although operated in CW mode. The 532 nm Raman laser

(Verdi, Coherent) was focused by a 50× microscope objective to a 1.6 μm spot size (fwhm) using a colinear geometry. The Raman signal was collected by the same imaging system as the CW photoluminescence experiment. A 533 nm notch filter (Thorlabs) with a 17 nm bandwidth was used to filter the fundamental laser frequency and obtain both Stokes and anti-Stokes peaks; 0.3 mW of Raman laser power for 120 s of exposure was used for all Raman versus photoexcitation measurements.

Electronic Band Structure Theory. The electronic structure and phonon calculations were performed using DFT as implemented in the open source code Quantum ESPRESSO.³⁹ We used plane-wave, fully relativistic pseudopotentials with nonlinear core correction. The exchange-correlation energy was described by the generalized gradient approximation (GGA), in the scheme proposed by Perdew, Burke, and Ernzerhof intended for solid-state and surface systems (PBEsol).⁴⁰ The cutoff energy used was 70 Ry. The Brillouin zone (BZ) was sampled for integrations according to the scheme proposed by Monkhorst and Pack⁴¹ with a grid of 14 × 14 × 1 *k*-points. The out-of-plane lattice constant *c* was set at 25 Å in a slab geometry to consider the monolayer system. The in-plane lattice parameter was determined by minimization of the total energy for the monolayers and was found to be 3.1492 Å. A biaxial tensile strain was introduced by varying the in-plane lattice constant *a*. For each strain/lattice expansion, the *z* coordinates of the chalcogen atoms were optimized and subsequently the electronic structure was calculated. The phonon frequencies were evaluated for each strain/lattice expansion at the Γ point. The variation of the Raman-active in-plane E' and out-of-plane A_1 modes was evaluated for comparison to the Raman spectroscopy measurements.

Time-Resolved Differential Transmission. Time-resolved differential transmission was performed using the same photoexcitation laser (637 nm) and pulse width (500 ns) that were used in the trPL experiment. White light from an optical parametric amplifier (OPA 9400, Coherent) pumped by an amplified femtosecond laser (RegA 9000, Coherent) was used as the transmission (“probe”) signal. The probe light (200 fs pulses at a 10 kHz repetition rate) was focused by a 50× microscope objective to a 1.6 μm spot size (fwhm) using a colinear geometry with respect to the photoexcitation laser. After passing through the sample and exiting the vacuum chamber, the probe light was collected by a 50× microscope objective and imaged onto the entrance slit of an integrated CCD spectrometer (Fergie, Princeton Instruments). Operating in kinetics spectroscopy mode, the Fergie was electronically triggered by the 10 kHz RegA source, thus acquiring each probe pulse. Externally triggered by the RegA source, a DG535 triggered the photoexcitation laser at 5 kHz with an adjustable time delay relative to the probe light. The output from this configuration was a 10 kHz probe (white light, 200 fs) with a 5 kHz photoexcitation (637 nm, 500 ns) with phase adjustability provided by the DG535 instrument. For each time step, alternating probe and pump+probe spectra from the Fergie were recorded and then processed to give $\Delta T/T$. Time sweeping was provided by the DG535 instrument by adjusting the relative time between the pump and probe. Every time step in Figure 3a is averaged over $\sim 750 \Delta T/T$ spectra. Although the timing system was capable of 20 ps resolution, the experimental timing was limited by the laser rise/fall time (2 ns). See Figure S8 for the experimental diagram.

■ ASSOCIATED CONTENT

📄 Supporting Information

The Supporting Information is available free of charge on the ACS Publications website at DOI: 10.1021/acs.nanolett.8b04408.

Low-power photoluminescence evolution, reproducibility, charge density measurement from bandgap renormalization (BGR), material temperature from Raman analysis, heat diffusion model, experimental diagrams, and additional references (PDF)

■ AUTHOR INFORMATION

Corresponding Author

*E-mail: kenan_gundogdu@ncsu.edu.

ORCID

Avinash Rustagi: 0000-0001-6776-9496

Alexander Kemper: 0000-0002-5426-5181

Linyou Cao: 0000-0002-7834-8336

Kenan Gundogdu: 0000-0001-7149-5766

Author Contributions

K.G., A.W.B., and R.A.Y. designed the research. L.C. and Y.Y. provided the samples. A.W.B. and R.A.Y. performed the optical and Raman measurements and analyzed the experimental data. A.K. and A.R. performed the theoretical calculations. A.W.B. drafted the manuscript with K.G. and received contributions from all authors.

Notes

The authors declare no competing financial interest.

■ ACKNOWLEDGMENTS

The authors acknowledge funding from the United States Army Research Office Grant W911NF-17-1-0483 and the National Science Foundation Grant DMR-1709934 and the OBIS laser gift from Coherent Lasers.

■ REFERENCES

- (1) Feng, J.; Qian, X.; Huang, C.-W.; Li, J. *Nat. Photonics* **2012**, *6* (12), 866.
- (2) Klots, A.; Newaz, A.; Wang, B.; Prasai, D.; Krzyzanowska, H.; Lin, J.; Caudel, D.; Ghimire, N.; Yan, J.; Ivanov, B.; et al. *Sci. Rep.* **2015**, *4*, 6608.
- (3) Yu, Y.; Yu, Y.; Cai, Y.; Li, W.; Gurarlan, A.; Peelaers, H.; Aspnes, D. E.; Van de Walle, C. G.; Nguyen, N. V.; Zhang, Y.-W.; Cao, L. *Sci. Rep.* **2015**, *5*, 16996.
- (4) Yu, Y.; Bataller, A.; Younts, R.; Yu, Y.; Li, G.; Puzos, A. A.; Geoghegan, D. B.; Gundogdu, K.; Cao, L. *arXiv* **2017**, 1710.09538.
- (5) Rustagi, A.; Kemper, A. F. *Nano Lett.* **2018**, *18* (1), 455–459.
- (6) Arp, T. B.; Pleskot, D.; Aji, V.; Gabor, N. M. *arXiv* **2017**, 1711.06917.
- (7) Jeffries, C. D.; Keldysh, L. u. d. V. *Electron-Hole Droplets in Semiconductors*; North Holland, 1983; Vol. 6.
- (8) Pokrovskii, Y. E.; Svistunova, K. *ZhETF Pisma Redaktsiiu* **1969**, *9*, 435.
- (9) Smith, L.; Wolfe, J. *Phys. Rev. B: Condens. Matter Mater. Phys.* **1995**, *51* (12), 7521.
- (10) Shimano, R.; Nagai, M.; Horiuchi, K.; Kuwata-Gonokami, M. *Phys. Rev. Lett.* **2002**, *88* (5), 057404.
- (11) Tränkle, G.; Lach, E.; Forchel, A.; Ell, C.; Haug, H.; Weimann, G.; Griffiths, G.; Kroemer, H.; Subbanna, S. *J. Phys., Colloq.* **1987**, *48* (C5), C5-385–C5-388.
- (12) Radisavljevic, B.; Radenovic, A.; Brivio, J.; Giacometti, i. V.; Kis, A. *Nat. Nanotechnol.* **2011**, *6* (3), 147.

- (13) Amani, M.; Lien, D.-H.; Kiriya, D.; Xiao, J.; Azcatl, A.; Noh, J.; Madhupathy, S. R.; Addou, R.; Santosh, K.; Dubey, M.; et al. *Science* **2015**, *350* (6264), 1065–1068.
- (14) Yu, Y.; Yu, Y.; Xu, C.; Barrette, A.; Gundogdu, K.; Cao, L. *Phys. Rev. B: Condens. Matter Mater. Phys.* **2016**, *93* (20), 201111.
- (15) Chakraborty, B.; Bera, A.; Muthu, D. V. S.; Bhowmick, S.; Waghmare, U. V.; Sood, A. K. *Phys. Rev. B: Condens. Matter Mater. Phys.* **2012**, *85* (16), 161403.
- (16) Rice, C.; Young, R. J.; Zan, R.; Bangert, U.; Wolverson, D.; Georgiou, T.; Jalil, R.; Novoselov, K. S. *Phys. Rev. B: Condens. Matter Mater. Phys.* **2013**, *87* (8), 081307.
- (17) Lloyd, D.; Liu, X.; Christopher, J. W.; Cantley, L.; Wadehra, A.; Kim, B. L.; Goldberg, B. B.; Swan, A. K.; Bunch, J. S. *Nano Lett.* **2016**, *16* (9), 5836–41.
- (18) Lu, P.; Wu, X.; Guo, W.; Zeng, X. C. *Phys. Chem. Chem. Phys.* **2012**, *14* (37), 13035–40.
- (19) Pan, H.; Zhang, Y.-W. *J. Phys. Chem. C* **2012**, *116* (21), 11752–11757.
- (20) Conley, H. J.; Wang, B.; Ziegler, J. I.; Haglund, R. F., Jr.; Pantelides, S. T.; Bolotin, K. I. *Nano Lett.* **2013**, *13* (8), 3626–30.
- (21) Mak, K. F.; Lee, C.; Hone, J.; Shan, J.; Heinz, T. F. *Phys. Rev. Lett.* **2010**, *105* (13), 136805.
- (22) Shi, H.; Yan, R.; Bertolazzi, S.; Brivio, J.; Gao, B.; Kis, A.; Jena, D.; Xing, H. G.; Huang, L. *ACS Nano* **2013**, *7* (2), 1072–1080.
- (23) Mai, C.; Barrette, A.; Yu, Y.; Semenov, Y. G.; Kim, K. W.; Cao, L.; Gundogdu, K. *Nano Lett.* **2014**, *14* (1), 202–6.
- (24) Zhu, Z. Y.; Cheng, Y. C.; Schwingenschlögl, U. *Phys. Rev. B: Condens. Matter Mater. Phys.* **2011**, *84* (15), 153402.
- (25) Pogna, E. A.; Marsili, M.; De Fazio, D.; Dal Conte, S.; Manzoni, C.; Sangalli, D.; Yoon, D.; Lombardo, A.; Ferrari, A. C.; Marini, A.; Cerullo, G.; Prezzi, D. *ACS Nano* **2016**, *10* (1), 1182–8.
- (26) Chernikov, A.; Ruppert, C.; Hill, H. M.; Rigosi, A. F.; Heinz, T. F. *Nat. Photonics* **2015**, *9* (7), 466–470.
- (27) Sie, E. J.; Frenzel, A. J.; Lee, Y.-H.; Kong, J.; Gedik, N. *Phys. Rev. B: Condens. Matter Mater. Phys.* **2015**, *92* (12), 125417.
- (28) Korn, T.; Heydrich, S.; Hirmer, M.; Schmutzler, J.; Schüller, C. *Appl. Phys. Lett.* **2011**, *99* (10), 102109.
- (29) Tongay, S.; Zhou, J.; Ataca, C.; Lo, K.; Matthews, T. S.; Li, J.; Grossman, J. C.; Wu, J. *Nano Lett.* **2012**, *12* (11), 5576–80.
- (30) Wang, X. H.; Ning, J. Q.; Su, Z. C.; Zheng, C. C.; Zhu, B. R.; Xie, L.; Wu, H. S.; Xu, S. J. *RSC Adv.* **2016**, *6* (33), 27677–27681.
- (31) He, Z.; Wang, X.; Xu, W.; Zhou, Y.; Sheng, Y.; Rong, Y.; Smith, J. M.; Warner, J. H. *ACS Nano* **2016**, *10* (6), 5847–55.
- (32) Najmaei, S.; Yuan, J.; Zhang, J.; Ajayan, P.; Lou, J. *Acc. Chem. Res.* **2015**, *48* (1), 31–40.
- (33) Tongay, S.; Suh, J.; Ataca, C.; Fan, W.; Luce, A.; Kang, J. S.; Liu, J.; Ko, C.; Raghunathan, R.; Zhou, J.; et al. *Sci. Rep.* **2013**, *3*, 2657.
- (34) Kang, N.; Paudel, H. P.; Leuenberger, M. N.; Tetard, L.; Khondaker, S. I. *J. Phys. Chem. C* **2014**, *118* (36), 21258–21263.
- (35) Nan, H.; Wang, Z.; Wang, W.; Liang, Z.; Lu, Y.; Chen, Q.; He, D.; Tan, P.; Miao, F.; Wang, X.; Wang, J.; Ni, Z. *ACS Nano* **2014**, *8* (6), 5738–5745.
- (36) Gutiérrez, H. R.; Perea-López, N.; Elías, A. L.; Berkdemir, A.; Wang, B.; Lv, R.; López-Urías, F.; Crespi, V. H.; Terrones, H.; Terrones, M. *Nano Lett.* **2013**, *13* (8), 3447–3454.
- (37) He, Z.; Wang, X.; Xu, W.; Zhou, Y.; Sheng, Y.; Rong, Y.; Smith, J. M.; Warner, J. H. *ACS Nano* **2016**, *10* (6), 5847–5855.
- (38) Haug, A. *Solid State Commun.* **1977**, *22* (8), 537–539.
- (39) Giannozzi, P.; Baroni, S.; Bonini, N.; Calandra, M.; Car, R.; Cavazzoni, C.; Ceresoli, D.; Chiarotti, G. L.; Cococcioni, M.; Dabo, I.; et al. *J. Phys.: Condens. Matter* **2009**, *21* (39), 395502.
- (40) Perdew, J. P.; Ruzsinszky, A.; Csonka, G. I.; Vydrov, O. A.; Scuseria, G. E.; Constantin, L. A.; Zhou, X.; Burke, K. *Phys. Rev. Lett.* **2008**, *100* (13), 136406.
- (41) Monkhorst, H. J.; Pack, J. D. *Phys. Rev. B* **1976**, *13* (12), 5188.